Supplementary Information

Unraveling the origin of conductivity change in Co-doped FeRh phase transition

Ji-Ho Park[1†], Min Tae Park[2†], Geon-Woo Baek[1†], Shin-ichi Kimura[3,4,5], Myung-Hwa Jung[2★], Kab-Jin Kim[1,6★]

[1]*Department of Physics, KAIST, Daejeon 34131, Republic of Korea*

[2]*Department of Physics, Sogang University, Seoul 04107, Republic of Korea*

[3]*Graduate School of Frontier Biosciences, Osaka University, Suita 565-0871, Japan*

[4]*Department of Physics, Graduate School of Science, Osaka University, Toyonaka 560-0043, Japan*

[5]*Institute for Molecular Science, Okazaki 444-8585, Japan*

[6]*Graduate School of Quantum Science and Technology, KAIST, Daejeon 34141, Republic of Korea*

Table of Contents

Supplementary Note 1. Sample characterization (XRD, EDS)

Supplementary Fig. 1(a) depicts the result of X-ray diffraction (XRD) $\theta - 2\theta$ measurement, which reveals the crystal structure of Co-doped FeRh. We clearly observe diffraction peaks from BCC α' FeRh (001) and (002), in addition to the peak from MgO (002) substrate. Note that Co doping does not affect the diffraction pattern of FeRh. The distribution of Fe, Rh, and Co has been confirmed by scanning electron microscopy-energy dispersive X-ray spectroscopy (EDS). Small amount of Co doping is evident in Supplementary Fig. 1(b). The exact composition of Fe, Rh and Co is shown in the table below Supplementary Fig. 1(b).

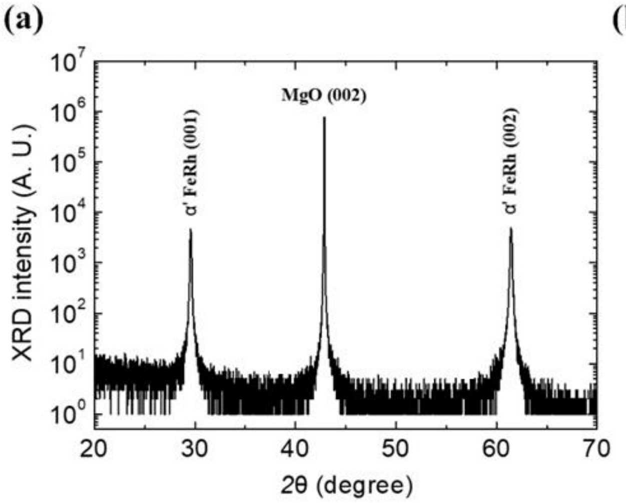

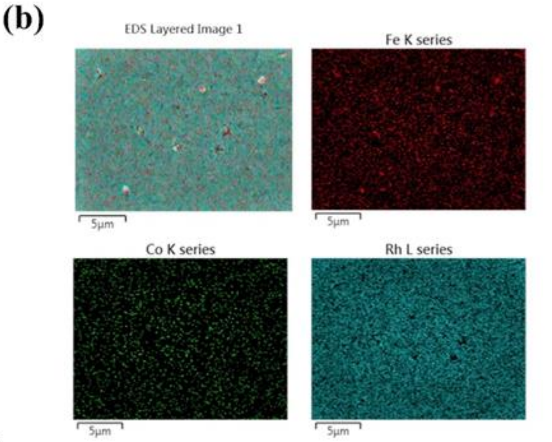

Element	Line Type	Wt %	Wt % (1σ)	Atomic %
Fe	K series	37.86	0.27	52.54
Co	K series	1.14	0.22	1.51
Rh	L series	61.00	0.29	45.95

Supplementary Figure 1. (a) XRD $\boldsymbol{\theta - 2\theta}$ scan for MgO/$Fe_{52.54}Rh_{45.95}Co_{1.51}$ (73 nm) / SiO_x (2 nm). (b) EDS images of surface of $Fe_{52.54}Rh_{45.95}Co_{1.51}$ (73 nm).

Supplementary Note 2. Magnetic contribution to the THz response

The magnetic properties of FeRh could influence the THz response if the magnetic field component of the THz wave couples with the material's magnetic properties. To investigate this possibility, we conducted THz measurements under an applied magnetic field (note that the measurements in the main text were performed without any external magnetic field).

The inset of Supplementary Fig. 2 illustrates the measurement setup, where the external magnetic field is aligned parallel to the magnetic field component of the THz wave, maximizing the potential coupling between the THz wave and the sample. Supplementary Fig. 2 compares the temperature-dependent THz peak amplitude in the presence (red) and absence (blue) of an external magnetic field.

The results indicate that the external magnetic field has a negligible effect, suggesting that the magnetic transition does not significantly influence the THz response. This minimal effect is likely due to the extremely small magnetic field component in our THz wave. In our THz-TDS setup, the magnitude of the THz electric field (E_{THz}) is 100 V/cm, while the THz magnetic field (B_{THz})) is only 0.033 mT, as $B_0 = \frac{E_0}{c}$. Consequently, the interaction between the THz wave and the sample is predominantly driven by the electric field component, with the magnetic contribution being insignificant.

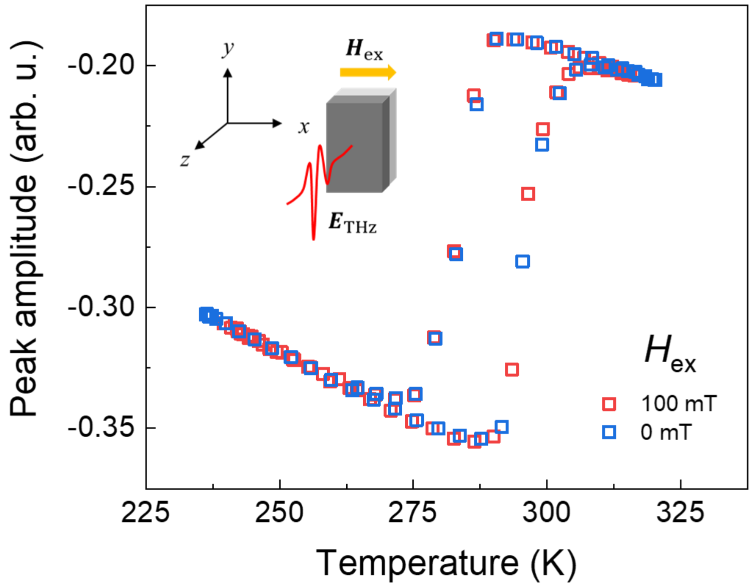

Supplementary Figure 2. Temperature-dependent THz peak amplitude in the presence (red) and absence (blue) of an external magnetic field. Inset: Schematic of the measurement setup, showing the direction of the applied external magnetic field, which is parallel to the magnetic field component of the THz wave.

Supplementary Note 3. Drude fitting & complex THz conductivities while decreasing temperature

Complex THz sheet conductivities for 6 selected temperatures while cooling from 335K are shown in Supplementary Fig. 3. Black and red points correspond to the real and imaginary parts of THz conductivities, respectively. Green lines on each graph are Drude fitting. All results are in good agreement with Drude model.

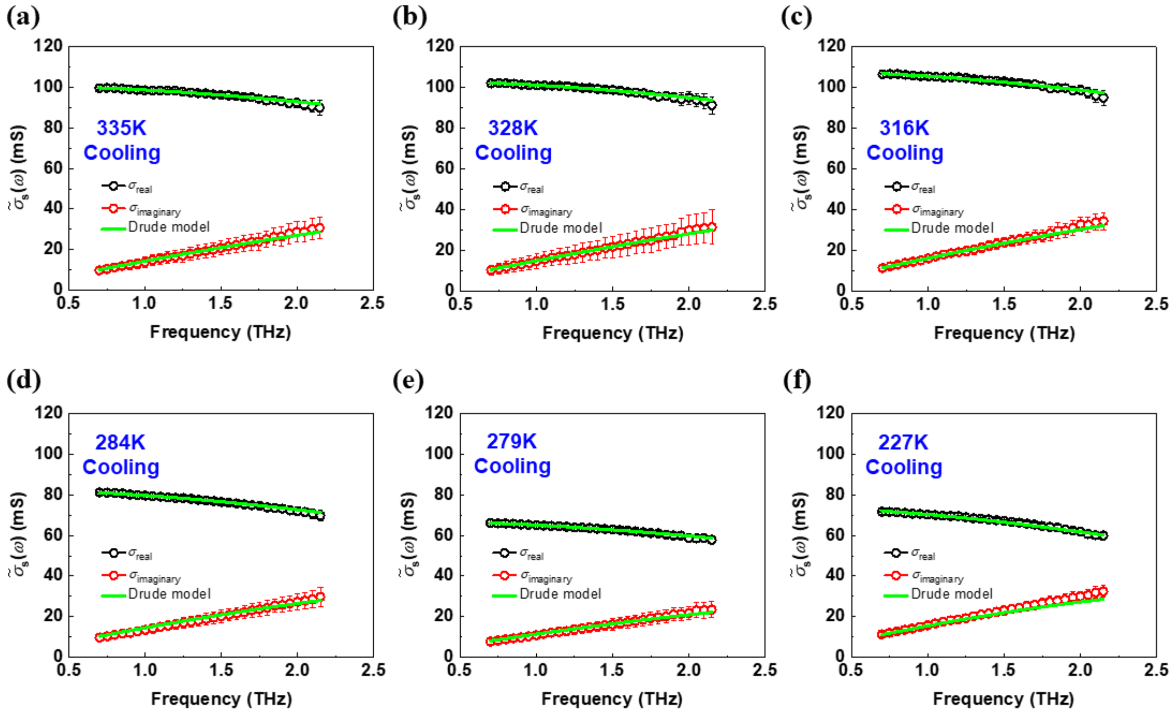

Supplementary Figure 3. Temperature-dependent complex THz sheet conductivities for (a) 335 K, (b) 328 K, (c) 316 K, (d) 284 K, (e) 279 K and (f) 227 K. Black (Red) data are real (imaginary) parts of THz conductivity. Green lines correspond to Drude fitting.

Supplementary Note 4. Drude fitting & complex THz conductivities while increasing temperature

Complex THz sheet conductivities for 6 selected temperatures while heating from 256K are shown in Supplementary Fig. 4.

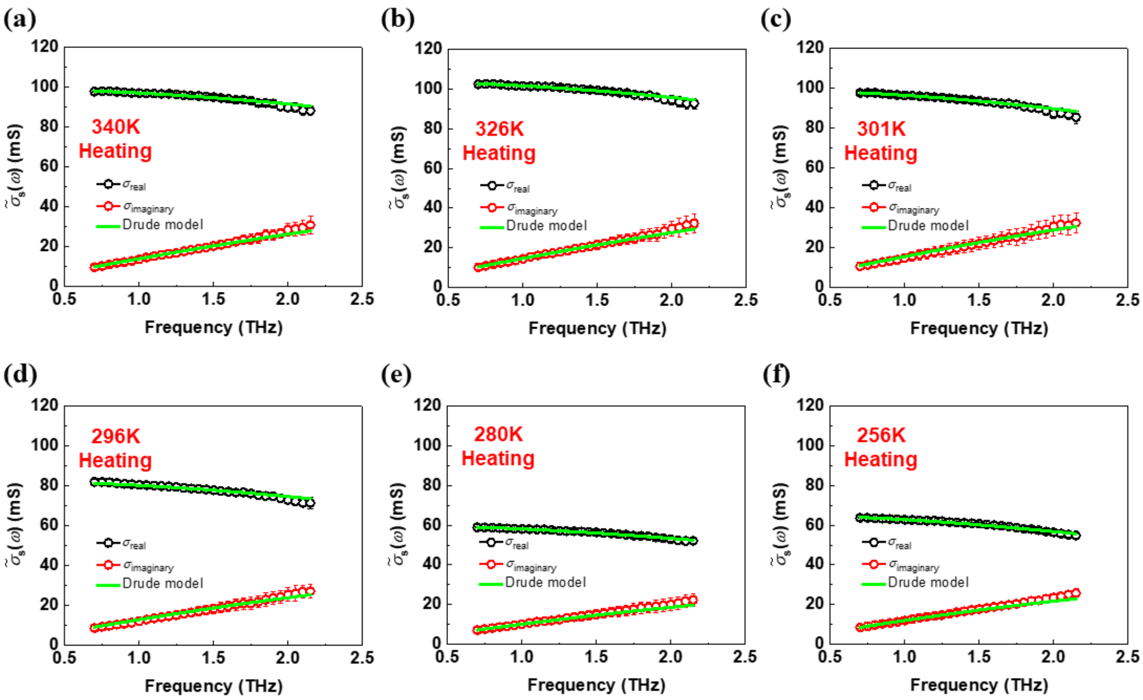

Supplementary Figure 4. Temperature-dependent complex THz sheet conductivities for (a) 340 K, (b) 326 K, (c) 306 K, (d) 296 K, (e) 280 K and (f) 256 K. Black (Red) data are real (imaginary) parts of THz conductivity. Green lines correspond to Drude fitting.

Supplementary Note 5. Contribution from high-frequency corrections due to optical phonons

In this section, we check the possible effect from high-frequency corrections due to optical phonons. The high-frequency contribution term can be expressed as: [1], [2]

$$\tilde{\sigma}_S(\omega) = \frac{d \cdot \sigma_{\mathrm{DC}}}{1 - i\omega\tau} - i(\epsilon_\infty - 1)\epsilon_0 \omega d \qquad \text{(S1)}$$

Supplementary Fig.5 and 6 show the THz sheet conductivity fitted with Eq. (S1) at various temperatures during the cooling and heating processes. The fitting parameters are summarized in Supplementary Fig. 7. The results obtained using Eq. (S1) show a very similar trend to those using simple Drude model (Fig. 3 of the manuscript), where τ gradually decreases monotonically with rising temperature (Supplementary Fig.7(b)), while a sharp change in n/m^* occurs during the phase transition (Supplementary Fig.7(c)). Therefore, even after considering the contribution of high-frequency excitations in the THz region, our main conclusion remains unchanged: the conductivity change in FeRh during the phase transition is predominantly due to an intrinsic origin.

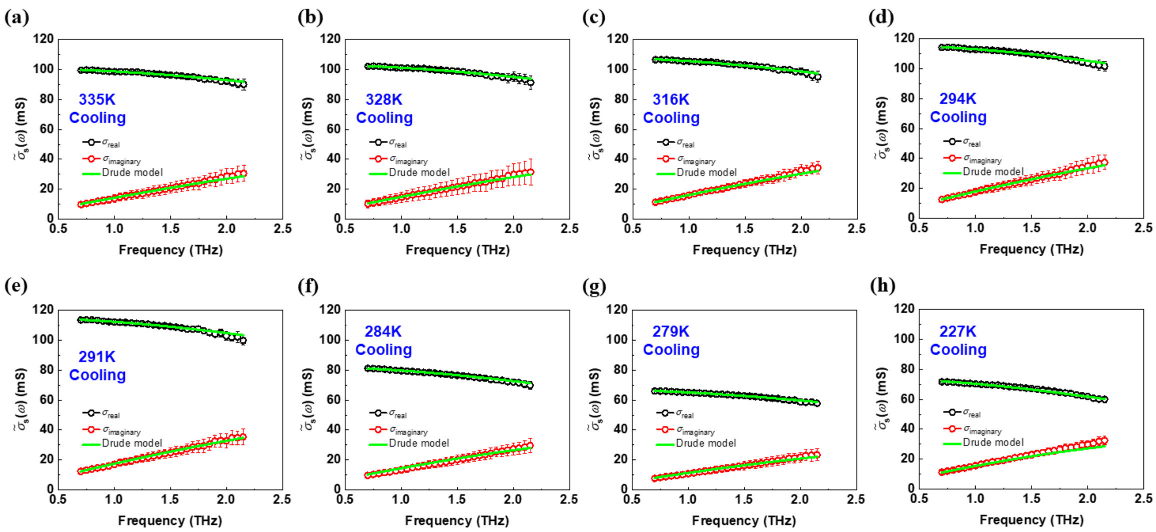

Supplementary Figure 5. Temperature-dependent complex THz sheet conductivities for (a) 335 K, (b) 328 K, (c) 316 K, (d) 294 K, (e) 291 K, (f) 284K, (g) 279K and (h) 227 K in cooling process. Black (Red) data are real (imaginary) parts of THz conductivity. Green lines correspond to modified Drude fitting.

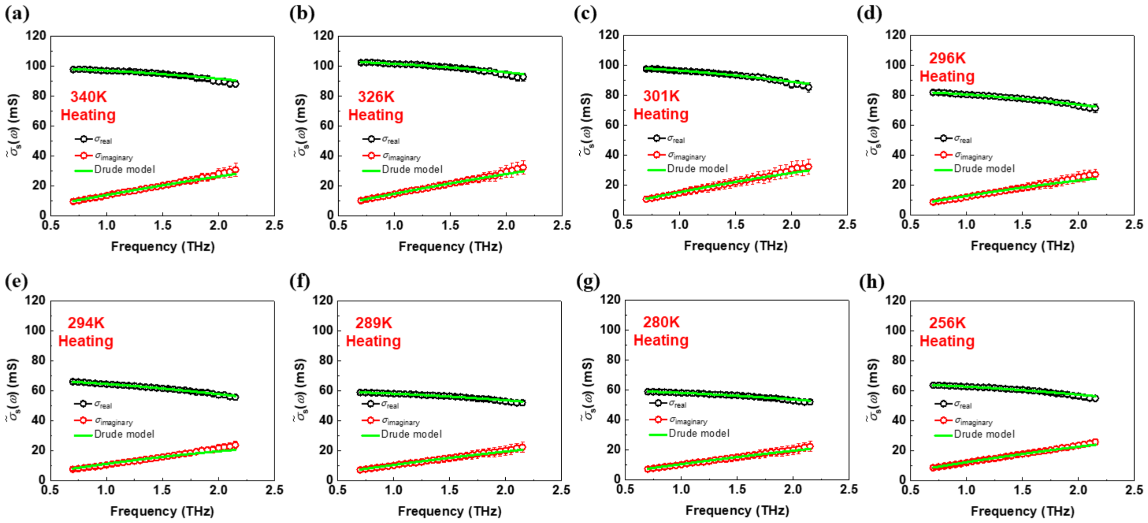

Supplementary Figure 6. Temperature-dependent complex THz sheet conductivities for (a) 340 K, (b) 326 K, (c) 301 K, (d) 296 K, (e) 294 K, (f) 289K, (g) 280K and (h) 256 K in heating process. Black (Red) data are real (imaginary) parts of THz conductivity. Green lines correspond to modified Drude fitting.

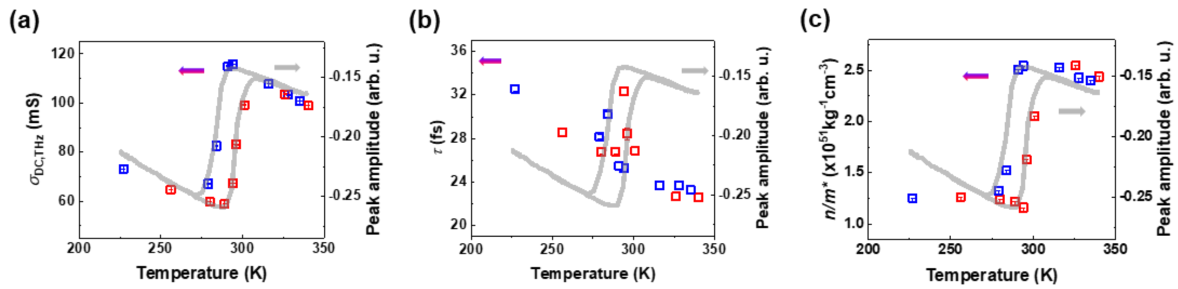

Supplementary Figure 7. Temperature-dependent negative pulse peak amplitude (gray line) compared with (a) the DC sheet conductivity $Re[\tilde{\sigma}_S(0)] \equiv \sigma_{\mathrm{DC}}$ (b) extrinsic contribution, τ and (c) intrinsic contribution, n/m^* obtained by analyzing complex THz conductivity based on the modified Drude model. Cooling data are represented in blue, while heating data are shown in red.

Supplementary Note 6. Temperature-dependent reflectivity spectra of Co-doped FeRh thin film.

Supplementary Fig. 8 is the temperature-dependent infrared (IR) reflectivity spectra of the FeRh thin film. The thin film was evaporated on a MgO substrate and covered by PMMA, so the obtained spectra are very complex. However, since the optical spectra of the MgO substrate and the PMMA film have no temperature dependence, the change in temperature originates from FeRh.

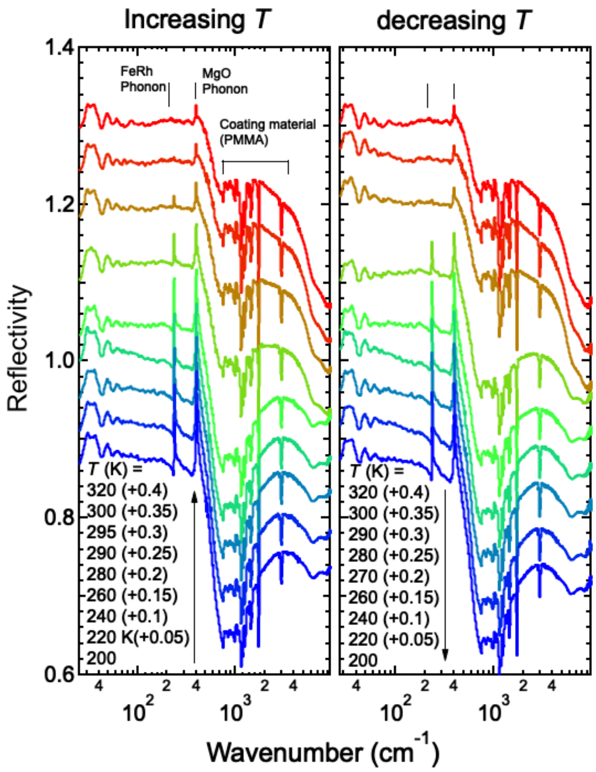

Supplementary Figure 8. Heating and cooling dependence of the reflectivity spectrum of a Co-doped FeRh thin film. Since the film is fabricated on a MgO substrate and the surface is protected by a PMMA film, the peaks originating from these materials appear in the spectra.

Supplementary References

[1] Wu, L. *et al*. A sudden collapse in the transport lifetime across the topological phase transition in (Bi1−xInx)2Se3. *Nature Phys* **9**, 410–414 (2013)

[2] Lv, Y. *et al*. Ultrafast THz emission spectroscopy of spin currents in the metamagnet FeRh. *APL Mater*. **12**, 041121 (2024)